Sensors & Actuators: B. Chemical 444 (2025) 138443

Contents lists available at ScienceDirect

Sensors and Actuators: B. Chemical

journal homepage: www.elsevier.com/locate/snb

Activatable near-infrared fluorogenic probe for monitoring GSH variations in synergistic PTX and RSL3 treatment of hypopharyngeal carcinoma

Yongzhi Qi [a,b,1], Cuijuan Zhang [c,1], Chenxiao Zhao [a,b], Yuxia Zou [a], Ziyi Cheng [a,b], Heng Liu [a,b,*], Xuejun Zhou [a,**], Fabiao Yu [a,b,*]

[a] Key Laboratory of Haikou Trauma, Key Laboratory of Hainan Trauma and Disaster Rescue, Key Laboratory of Emergency and Trauma of Ministry of Education, Department of Otolaryngology, Head and Neck Surgery, The First Affiliated Hospital of Hainan Medical University, Hainan Medical University, Haikou 571199, China
[b] Engineering Research Center for Hainan Bio-Smart Materials and Bio-Medical Devices, Key Laboratory of Hainan Functional Materials and Molecular Imaging, College of Emergency and Trauma, Hainan Medical University, Haikou 571199, China
[c] Department of Cardiovascular Surgery, First Center of 301 Chinese PLA General Hospital, Beijing 100853, China

ARTICLE INFO

Keywords:
Glutathione
Near-infrared fluorogenic probe
Ferroptosis
Hypopharyngeal carcinoma
Therapy monitoring

ABSTRACT

Hypopharyngeal carcinoma (HPC) is a class of rare squamous cell carcinomas of the head and neck that are highly aggressive and have a poor prognosis. It is mostly clinically diagnosed at an advanced stage and is pronounced resistant to chemotherapy. Ferroptosis, a class of iron-dependent programmed cell death triggered by lipid peroxidation accumulation, is regarded as a novel strategy for antitumor therapy. In this work, a novel GSH-activatable near-infrared fluorogenic (NIRF) probe, DCI-F, was screened based on a substituent-regulation strategy. This probe was successfully applied to the study of ferroptosis induced by the combination of low-dose PTX and RSL3, which demonstrated that the combination therapy synergistically accelerated GSH depletion in tumor cells. DCI-F was able to distinguish tumor cells from normal squamous cells. The combination of PTX + RSL3 reduced intratumorally GSH levels and enhanced the therapeutic efficacy compared to single-drug treatment in FaDu tumor-bearing mice model. DCI-F enabled deep tissue imaging in fresh specimens of HPC patient. This work provided a novel GSH imaging tool for the development of low-toxicity and efficient tumor synergistic treatment strategies.

1. Introduction

Hypopharyngeal carcinoma (HPC) is a rare malignant tumor of the head and neck originating from the squamous epithelium, with a higher incidence in Asia than in other regions [1]. The disease appears to be gender-specific, with males being at higher risk of developing the disease and having a lower survival rate [2]. Due to the absence of typical clinical symptoms in the early stages, most patients are diagnosed in advanced stages, often associated with cervical lymph node metastases [3,4]. Late-stage HPC is usually treated with a combination of surgery and radiotherapy [5]. Paclitaxel (PTX) is a commonly used first-line chemotherapeutic drug that interferes with microtubule function and induces cell cycle arrest [6,7]. Current strategies to overcome PTX resistance include inhibition of glutathione (GSH)-mediated regulation of reactive oxygen species (ROS), reduction of intracellular GSH levels to prevent drug efflux or metabolic inactivation, and activation of programmed cell death pathways [8,9].

Ferroptosis is a class of iron-driven programmed cell death modalities dependent on the accumulation of lipid peroxidation as the central mechanism, which is closely associated with the development of tumors [10–12]. GSH, a key molecule in maintaining intracellular redox homeostasis, is the main reducing substrate of glutathione peroxidase 4 (GPX4). Depletion of GSH or inactivation of GPX4 leads to an imbalance in the function of the antioxidant system, triggering the accumulation of lipid ROS and ferroptosis [13,14]. In the tumor microenvironment, GSH levels in malignant tissues are usually upregulated compared to normal

* Corresponding authors at: Key Laboratory of Haikou Trauma, Key Laboratory of Hainan Trauma and Disaster Rescue, Key Laboratory of Emergency and Trauma of Ministry of Education, Department of Otolaryngology, Head and Neck Surgery, The First Affiliated Hospital of Hainan Medical University, Hainan Medical University, Haikou 571199, China.
** Corresponding author.
E-mail addresses: liuheng11b@muhn.edu.cn (H. Liu), xuejunzhouent@muhn.edu.cn (X. Zhou), yufabiao@muhn.edu.cn (F. Yu).
[1] These authors contributed equally to this work (Y. Z. Qi and C. J. Zhang).

https://doi.org/10.1016/j.snb.2025.138443
Received 27 April 2025; Received in revised form 23 July 2025; Accepted 31 July 2025
Available online 4 August 2025

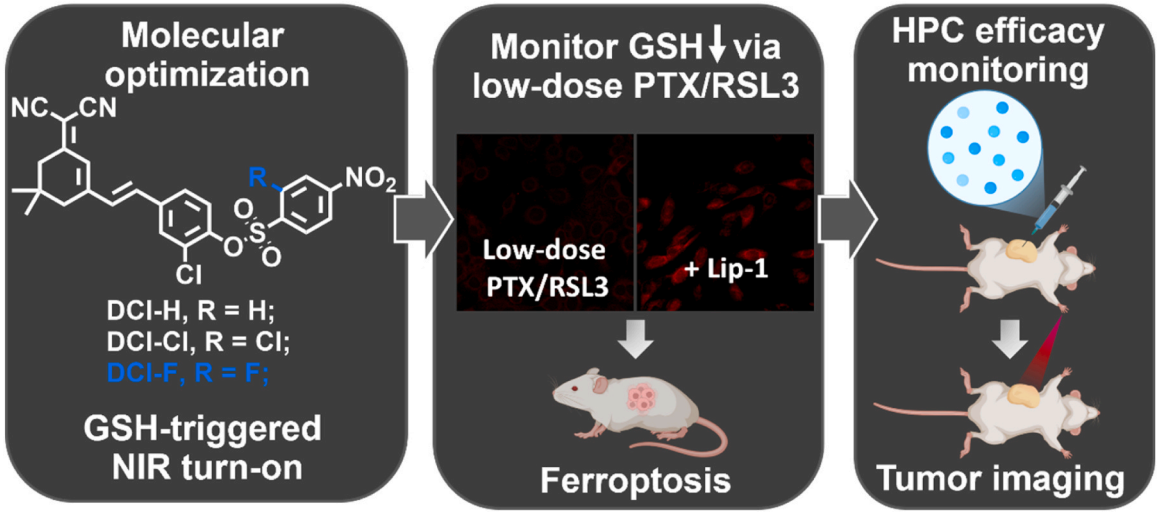

Scheme 1. Illustration of screening a GSH-activatable NIRF probe for visualizing ferroptosis induced by low-dose PTX/RSL3 and assessing HPC treatment efficacy (by BioRender).

tissues, enhancing chemotherapy tolerance and inhibiting ferroptosis signaling activation [15–17]. Hence, real-time monitoring of GSH dynamics in tumors is essential for clarifying the ferroptosis mechanism and accurately assessing the therapeutic efficacy.

Near-infrared fluorogenic (NIRF) probes have received widespread attention in the field of *in vivo* imaging owing to their advantages of deep tissue penetration, low background interference, and minimal photodamage [18–21]. In recent years, a variety of GSH-responsive fluorogenic probes have been developed based on different recognition moieties [22–31]. However, some of them are still limited to the visible light band, with poor selectivity and limited biological applications [32]. Herein, an activatable NIRF probe, DCI-F, was screened through substituent optimization of the recognition moiety based on dicyanoisophorone dye (Scheme 1). Employing DCI-F, endogenous GSH fluctuations during ferroptosis induced by the combination of low-dose PTX and RSL3 were visualized. Moreover, DCI-F was successfully applied to evaluate the efficacy of FaDu tumor-bearing mice of PTX+RSL3 combination therapy and to diagnostic imaging of HPC clinical specimens.

2. Experimental section

2.1. Materials and apparatus

The materials, instruments, fluorescence analysis, analytes solution preparation, cytotoxicity, cell culture, and cellular model were listed in the Supporting information.

2.2. Synthesis of (E)-2-chloro-4-(2-(3-(dicyanomethylene)-5,5-dimethylcyclohex-1-en-1-yl) vinyl) phenyl 2-fluoro-4-nitrobenzenesulfonate (DCI-F)

Compound DCI (65 mg, 0.2 mmol) was dissolved in dichloromethane, followed by the addition of 2-fluoro-4-nitrobenzenesulfonyl chloride (96 mg, 0.4 mmol) and triethylamine (0.2 mL) under stirring. The reaction was monitored by TLC until completion. The ice-cooled water was added to the reaction mixture, then extracted with dichloromethane, dried over anhydrous sodium sulfate, and concentrated under reduced pressure. The crude product was purified by silica gel column chromatography (EA/PE = 1/3) to afford DCI-F as a yellow solid (59 mg, yield: 56 %). ^{1}H NMR (400 MHz, $CDCl_3$): δ 8.15 (t, J = 7.1 Hz, 2 H), 8.10 (d, J = 7.6 Hz, 1 H), 7.52 (s, 1 H), 7.42 (s, 2 H), 6.92 (d, J = 4.2 Hz, 2 H), 6.87 (s, 1 H), 2.61 (s, 2 H), 2.43 (s, 2 H), 1.08 (s, 6 H); ^{13}C NMR (101 MHz, $CDCl_3$): 168.80, 152.29, 145.15, 136.53, 133.17, 132.42, 131.70, 129.31, 127.65, 126.85, 124.94, 119.38, 119.34, 113.62, 113.36, 113.06, 112.31, 80.24, 42.87, 39.10, 32.01, 27.95. HRMS m/z: $C_{25}H_{19}ClFN_3O_5S$ [M - H]$^-$ calcd for 526.0640 found 526.0667.

2.3. Synthesis of (E)-2-chloro-4-(2-(3-(dicyanomethylene)-5,5-dimethylcyclohex-1-en-1-yl) vinyl) phenyl 2-chloro-4-nitrobenzenesulfonate (DCI-Cl)

DCI-Cl was prepared from typical procedure (EA/PE = 1/3) as yellow solid (52 mg, 48 %). ^{1}H NMR (400 MHz, $CDCl_3$): δ 8.46 (t, J = 1.9 Hz, 1 H), 8.25–8.20 (m, 2 H), 7.52 (d, J = 1.9 Hz, 1 H), 7.39 (dd, J = 8.6, 1.9 Hz, 1 H), 7.33 (d, J = 8.6 Hz, 1 H), 6.94 (d, J = 16.2 Hz, 1 H), 6.89 (d, J = 16.3 Hz, 1 H), 6.86 (s, 1 H), 2.61 (s, 2 H), 2.42 (s, 2 H), 1.07 (s, 6 H); ^{13}C NMR (101 MHz, $CDCl_3$): 168.92, 152.42, 151.14, 145.49, 139.91, 136.58, 135.73, 133.31, 133.10, 131.78, 129.53, 127.97, 127.38, 126.87, 125.04, 124.96, 121.90, 113.18, 112.43, 80.34, 42.99, 39.22, 32.12, 28.07. HRMS m/z: $C_{25}H_{19}Cl_2N_3O_5S$ [M - H]$^-$ calcd for 542.0344 found 542.0403.

2.4. Synthesis of (E)-2-chloro-4-(2-(3-(dicyanomethylene)-5,5-dimethylcyclohex-1-en-1-yl) vinyl) phenyl 4-nitrobenzenesulfonate (DCI-H)

DCI-H was prepared from typical procedure (EA/PE = 1/3) as yellow solid (60 mg, 59 %). ^{1}H NMR (400 MHz, $CDCl_3$): 8.39 (d, J = 8.8 Hz, 2 H), 8.12 (d, J = 8.8 Hz, 2 H), 7.49–7.43 (m, 3 H), 6.93–6.87 (m, 3 H), 2.61 (s, 2 H), 2.43 (s, 2 H), 1.07 (s, 6 H); ^{13}C NMR (101 MHz, d_6-DMSO): 170.22, 154.87, 151.33, 144.37, 139.63, 137.29, 134.13, 132.22, 130.19, 129.17, 128.33, 126.98, 125.17, 124.50, 124.04, 113.65, 77.61, 42.21, 38.07, 31.70, 27.44; HRMS m/z: $C_{25}H_{20}ClN_3O_5S$ [M + Na]$^+$ calcd for 532.0710 found 532.0706.

2.4.1. In vivo fluorescence imaging in tumor-bearing BALB/c mice model

All surgical procedures and experimental protocols were approved by the Animal Care and Use Committee of Hainan Medical University (HYLL-2024–809). FaDu tumor-bearing BALB/c nude mice were randomly divided into four groups: control, PTX, RSL3, and PTX + RSL3. Drug formulations were prepared as follows: PTX was dissolved in DMSO to yield a stock solution of 0.1 mg/mL and administered intraperitoneally at 1 mg/kg; RSL3 was dissolved in DMSO to prepare a 0.5 mg/mL stock and administered intraperitoneally at 5 mg/kg. For PTX + RSL3 group, mice received consecutive injection of PTX (1 mg/

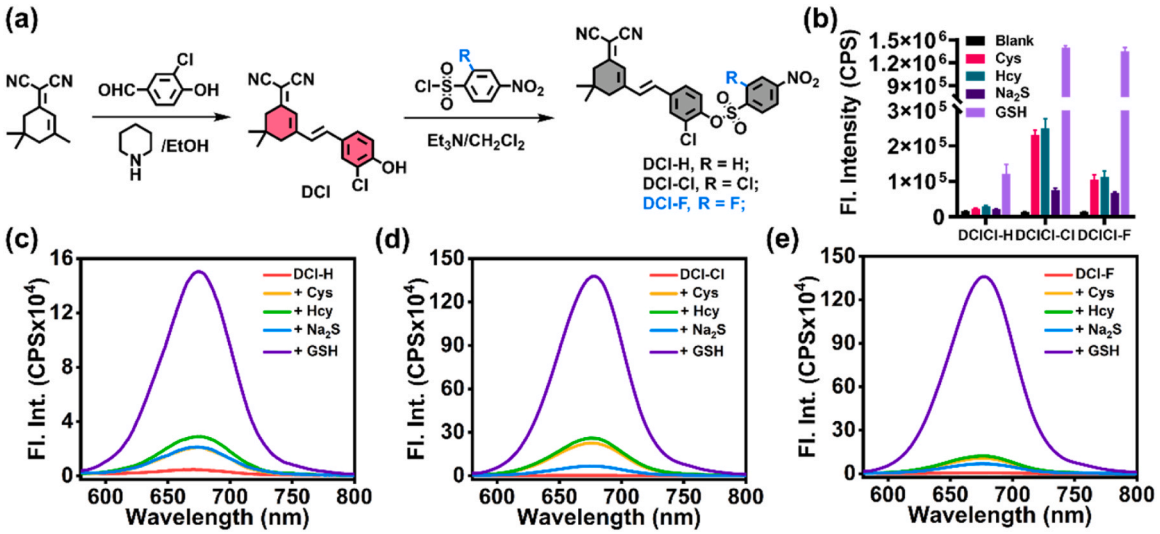

Fig. 1. (a) Synthetic route of NIRF probes DCI-H, DCI-Cl, and DCI-F. (b) Fluorescence intensity at 675 nm of DCI-H, DCI-Cl, and DCI-F upon treatment with various sulfur species (GSH, Cys, Hcy, Na_2S). (c) Fluorescence spectra of DCI-H (10 μM, c), DCI-Cl (10 μM, d), DCI-Cl (10 μM, e) in the presence of different sulfur species (GSH, Cys, Hcy, Na_2S). The final concentrations were 1 mM of GSH, 200 μM of Cys, 100 μM of Hcy, or Na_2S. $\lambda_{ex} = 560$ nm.

kg) and RSL3 (5 mg/kg) to ensure simultaneous action of the two drugs. The control group received vehicle alone under matched volumes. All treatments were administered every other day for a total of 14 days. All mice were administered DCI-F (100 μM, 50 μL) via intratumorally injection. Following anesthesia, *in vivo* fluorescence imaging was performed using IVIS Lumina XR small animal optical imaging system. The imaging parameters were set with an excitation wavelength of 535 nm, and fluorescence emission was recorded at 675 ± 20 nm. Tumor tissues were then fixed in 4 % paraformaldehyde, embedded in paraffin, and subjected to standard hematoxylin and eosin (H&E) staining for histopathological analysis.

3. Results and discussion

3.1. Molecular design

Substituent-regulation strategies have been widely employed to modulate electronic effects and spatial configuration of fluorogenic probes to optimize their response kinetics and recognition selectivity with specific biomarkers. In complex physiological environments, rational substituent design could improve the imaging performance of probes. In this design, three 4-nitrobenzene sulfonyl derivatives bearing different substituents (H, Cl, F) were introduced into the DCI dye scaffold to generate a series of NIRF probes DCI-H, DCI-Cl, and DCI-F

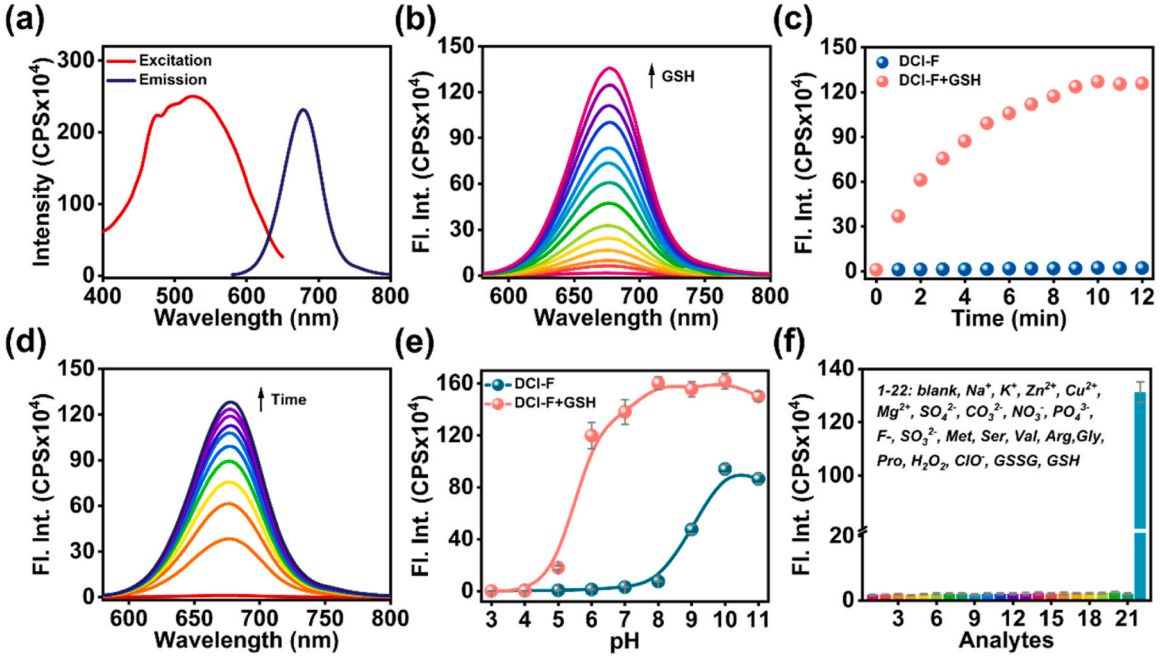

Fig. 2. (a) Excitation and emission spectra of the fluorescent dye DCI. (b) Fluorescence spectra of DCI-F (10 μM) after adding various concentrations of GSH (0–500 μM) for 10 min. (c) Fluorescence intensity of DCI-F (10 μM) before and after the addition of GSH (1 mM). (d) Time-dependent fluorescence spectra of DCI-F (10 μM) in the presence of GSH (1 mM). (e) Effects of pH on DCI-F (10 μM) for detection of GSH (1 mM). (f) Fluorescence response of DCI-F (10 μM) at 675 nm toward various representative biological species. 1. blank; 2–12: 100 μM of Na^+, K^+, Zn^{2+}, Cu^{2+}, Mg^{2+}, SO_4^{2-}, CO_3^{2-}, NO_3^-, PO_4^{3-}, F^-, SO_3^{2-}; 13–18: 1 mM of Met, Ser, Val, Arg, Gly, Pro; 19–21: 100 μM of H_2O_2, ClO^-, GSSG; 22: 1 mM of GSH. $\lambda_{ex} = 560$ nm.

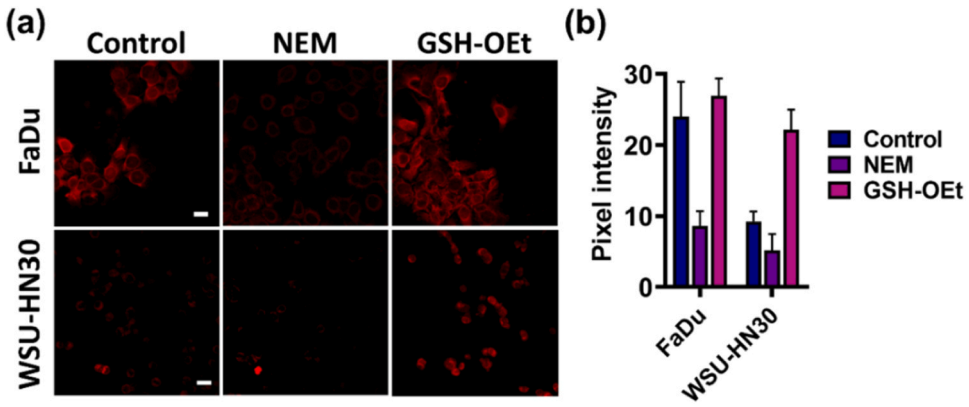

Fig. 3. Discrimination between FaDu and WSU-HN30 cells based on intracellular GSH levels. (a) Fluorescence imaging of FaDu and WSU-HN30 cells stained with DCI-F (10 μM) for 30 min. The cells were either untreated, pretreated with NEM (1 mM) for 15 min, or NEM (1 mM) for 15 min followed by GSH-OEt (1 mM) for another 15 min. Scale bars: 20 μm. (b) Pixel intensity of images in plane (a). The data are presented as mean ± s. d. (n = 3).

(Fig. 1a). The chemical structures of these compounds were confirmed by NMR and HRMS (Figure S1-S10). The selectivity of DCI-H, DCI-Cl, and DCI-F toward biological sulfur species (GSH, Cys, Hcy, H_2S) was then evaluated. The results in Figs. 1b-1e implied that DCI-H exhibited moderate selectivity for GSH but suffered from low detection sensitivity. The sensitivity of DCI-Cl was remarkably improved compared to DCI-H. However, its selectivity for GSH was compromised by interference from Cys and Hcy. Having comprehensively analyzed the effects of substituents on the reactivity of the DCI-H, DCI-Cl, and DCI-F with biological sulfur species, DCI-F was found to be the most suitable for *in vitro* and *in vivo* GSH imaging. To further clarify the sensing mechanism, the UV-Vis absorption spectra were compared (Figure S10). DCI-F exhibited a characteristic absorption peak centered at 375 nm, whereas the absorption peak of DCI was located at 535 nm. Upon reaction with GSH, the solution appeared both 375 nm and 535 nm absorption peaks, indicating the co-existence of DCI-F and DCI in the system. Moreover, HRMS indicated in the reaction system of DCI-F and GSH, two major peaks at at m/z 323.0963 and m/z = 526.0643, assigned to compound DCI ($[M - H]^-$) and DCI-F ($[M - H]^-$) respectively (Figure S12). These results verified that DCI-F could be specifically cleaved by GSH to release DCI dye.

3.2. Evaluation of the spectral properties of DCI-F

With DCI-F in hand, its performance in response to GSH in PBS (20 mM, containing 1 mM CTAB, pH 7.4) solution was investigated. The excitation and emission spectra of the fluorescent dye DCI were first tested. As shown in Fig. 2a, DCI presented a broad excitation band, and the maximum emission peak located at 675 nm. Based on this, 560 nm was chosen as the excitation wavelength in the subsequent experiments. Upon incremental addition of GSH, a gradual increase in the fluorescence of DCI-F was observed (Fig. 2b). Up to 500 μM GSH, the fluorescence intensity approached saturation (Figure S13a). Analysis displayed that fluorescence intensity at 675 nm of DCI-F was linearly correlated with GSH concentration in the range of 0–100 μM ($y = 6517.9 x + 16919$, $R^2 = 0.98$), and the limit of detection (LOD) was calculated to be 0.59 μM (Figure S13b). The reaction kinetics between DCI-F and GSH was further examined (Figs. 2c, 2d). Upon reacting with GSH, the fluorescence intensity of DCI-F progressively increased and reached a plateau period of approximately 10 min. To assess the adaptive range of DCI-F to pH, the fluorescence response of DCI-F to GSH at varied pH from 3.0 to 11.0 (Fig. 2e). DCI-F remained relatively stable at a pH less than 8.0; its fluorescence increased at a pH greater than 8.0, probably due to the alkaline environment inducing the hydrolysis of DCI-F and the release of the fluorescence product DCI. It was noteworthy that DCI-F exhibited a stable and strong fluorescence response to GSH across a wide pH range (4.0–11.0) and showed excellent fluorescence enhancement under physiological pH (7.4). In the end, the selectivity of DCI-F for GSH was evaluated by comparing its response with various representative biological species, including cations (Na^+, K^+, Zn^{2+}, Cu^{2+}, Mg^{2+}), anions (SO_4^{2-}, CO_3^{2-}, NO_3^-, PO_4^{3-}, F^-, SO_3^{2-}), amino acids (Met, Ser, Val, Arg, Gly, Pro), reactive oxygen species (H_2O_2, ClO^-), and sulfur species (GSSG, GSH). As depicted in Fig. 2f, fluorescence intensities of biological species were nearly identical to that of the blank. Only the addition of GSH produced a significantly enhanced fluorescence that was markedly higher than the blank and biological species. These results indicated that DCI-F could be selectively activated, suiting for sensitivity and specificity for GSH detection.

3.3. Imaging of endogenous GSH in live cells

Biosafety is a pivotal factor in the clinical translational application of molecular probes. To evaluate the biocompatibility of DCI-F, its cytotoxicity was measured in the concentration range of 0–50 μM using the CCK-8 assay. As illustrated in Figure S14, the cell viability of human hypopharyngeal squamous carcinoma cells (FaDu) and normal squamous epithelial cells (WSU-HN30) was maintained above 75 % even at the highest concentration of 50 μM after 24 h of treatment, indicative of the low toxicity of DCI-F, making it applicable for live cell imaging experiments. Afterward, DCI-F was incubated with FaDu and WSU-HN30 cells, respectively, and the intracellular fluorescence response to endogenous GSH was observed via confocal laser scanning microscopy (CLSM). As seen in Fig. 3a, WSU-HN30 cells, which possessed relatively low endogenous GSH levels, produced weak fluorescence after incubation with DCI-F. In contrast, FaDu cells exhibited significantly enhanced fluorescence due to high endogenous GSH levels. These results confirmed that DCI-F was able to effectively distinguish WSU-HN30 from FaDu cells based on differences in intracellular GSH levels. Moreover, treatment with N-ethylmaleimide (NEM) (a commercial thiol scavenger) resulted in a marked reduction in fluorescence in both cell types. When exogenously supplemented with GSH-OEt, a membrane-permeable GSH precursor hydrolyzed to GSH, the intracellular fluorescence was restored (Fig. 3b). This reversible response further validated the reliability and specificity of DCI-F as an activatable NIRF probe for intracellular GSH detection.

3.4. Real-time visualization of intracellular GSH dynamics in the process of RSL3-induced ferroptosis

Upon GSH depletion or impaired GPX4 function, the cellular antioxidant defense mechanism was imbalanced, thereby triggering ferroptosis [33,34]. As such, the reduction of GSH levels was considered to

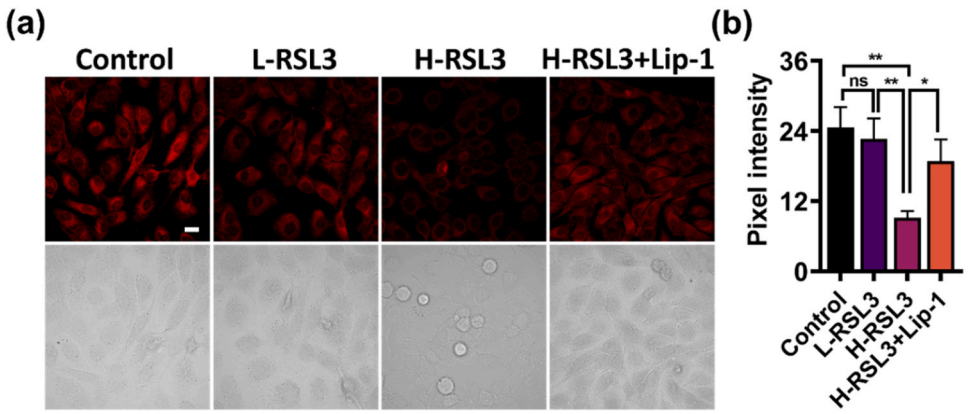

Fig. 4. Imaging of GSH dynamics during RSL3-induced ferroptosis. (a) Fluorescence imaging of FaDu cells loaded with DCI-F (10 μM) for 30 min. The cells were pretreated with L-RSL3 (0.25 μM), H-RSL3 (0.5 μM), or H-RSL3 (0.5 μM) + Lip-1 (0.1 μM) for 24 h. Scale bars: 20 μm. (b) Pixel intensity of images in plane (a). The data are presented as mean ± s. d. (n = 3). Statistical analysis was performed using a one-way ANOVA and multiple comparison test of significant differences ($^{*}P < 0.05$, $^{**}P < 0.01$).

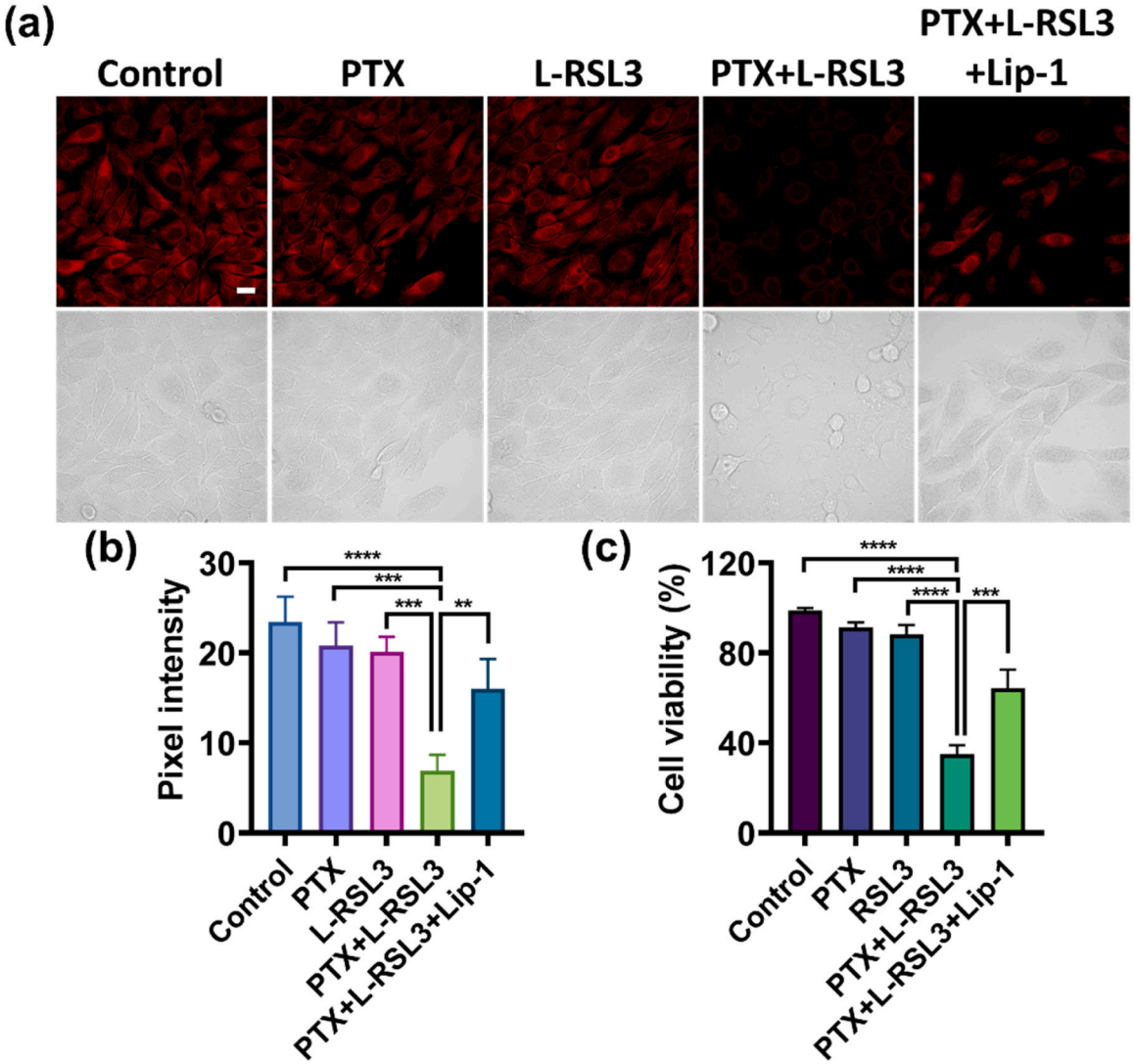

Fig. 5. Imaging of intracellular GSH under combination treatment with low-dose PTX and RSL3. (a) Fluorescence imaging of FaDu cells loaded with DCI-F (10 μM) for 30 min. The cells were pretreated with PTX (3 nM), L-RSL3 (0.25 μM), PTX (3 nM) + L-RSL3 (0.25 μM), PTX (3 nM) + L-RSL3 (0.25 μM) + Lip-1 (0.1 μM) for 24 h. Scale bars: 20 μm. (b) Pixel intensity of images in panel (a). (c) Cell viability of different groups in panel (a). The data are presented as mean ± s. d. (n = 3). λ_{ex} = 561 nm. Statistical analysis was performed using a one-way ANOVA and multiple comparison test of significant differences ($^{**}P < 0.01$, $^{***}P < 0.001$, $^{****}P < 0.0001$).

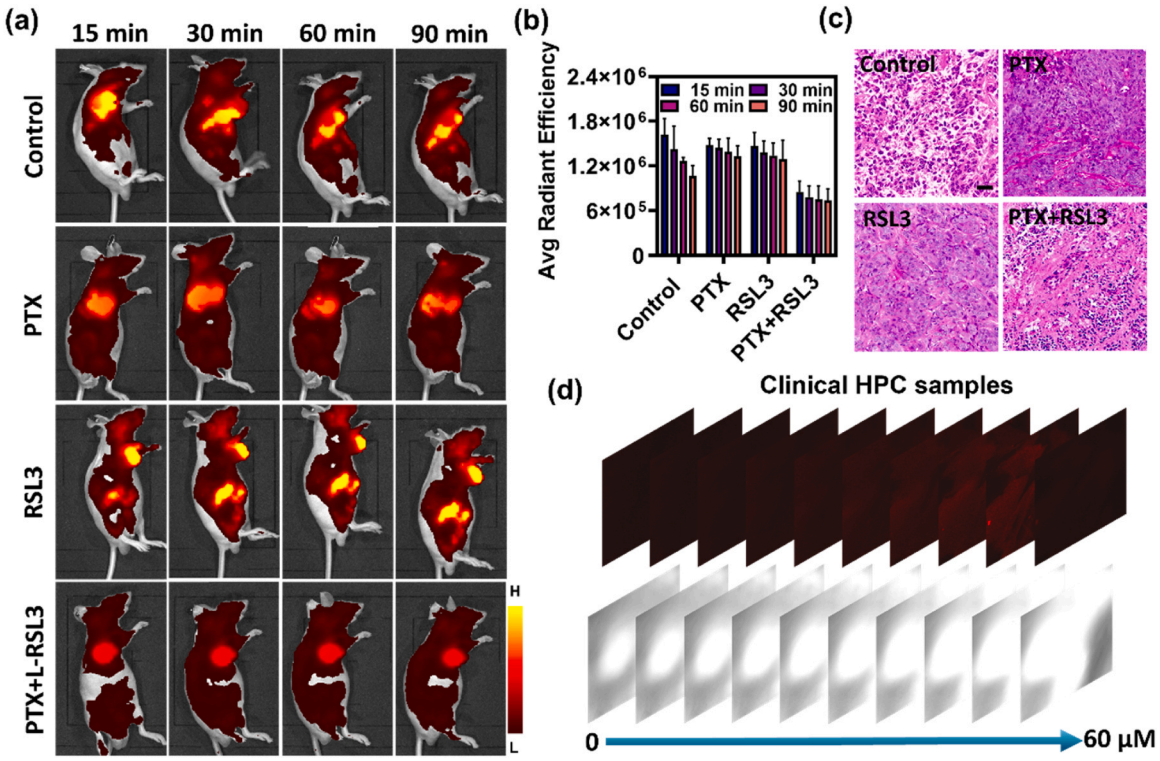

Fig. 6. *In vivo* imaging and treatment evaluation of FaDu tumor-bearing mice. (a) Fluorescence images of tumor-bearing mice within 90 min post-intratumorally injection of DCI-F (100 μM, 50 μL) in four groups: control, PTX, RSL3, PTX + RSL3. (b) Average radiant efficiency in the mice's tumor region corresponding to panel (a). (c) H&E staining images of the tumor tissues from each group. Scale bar: 150 μm. (d) NIRF imaging of freshly frozen HPC tissue. Confocal z-stack images acquired at penetration depths of 0 - 60 μm. The data are presented as mean ± s. d. (n = 3).

be one of the key drivers for the onset of ferroptosis and was also widely regarded as an important biomarker for assessing this process [35]. To verify this mechanism, FaDu cells were treated with various concentrations of RSL3 (a GPX4-specific inhibitor) for 24 h (Fig. 4a). High-dose RSL3 (H-RSL3) treatment greatly reduced the intracellular fluorescence intensity, indicative of a decrease in GSH levels. In contrast, low-dose RSL3 (L-RSL3) treatment did not elicit noticeable changes, implying that the ferroptosis pathway was not sufficiently activated at this concentration. It was noteworthy that the fluorescence intensity was significantly restored upon the addition of ferroptosis inhibitor liproxstatin-1 (Lip-1), illustrating that Lip-1 was effective in blocking GSH depletion induced by H-RSL3 (Fig. 4b). The cytotoxicity of various concentrations of RSL3 was further evaluated. As presented in Figure S15, cell viability showed a decreasing trend with increasing RSL3 concentration. Of which, no significant cell death was observed in the L-RSL3 group, while substantial cytotoxicity was detected in the H-RSL3 group. These findings demonstrated that H-RSL3 could induce a decrease in GSH levels and cell death via the activation of ferroptosis, whereas L-RSL3 was not sufficient to trigger this process alone.

3.5. Fluorescence imaging reveals synergistic ferroptosis induction by low-dose PTX and RSL3 in FaDu cells

Although PTX was a classical chemotherapeutic agent, high doses were usually required for efficacy in hypopharyngeal squamous cell carcinoma, which was often paired with strong toxic side effects [36]. Thus, exploring combination strategies to enhance efficacy under low-dose conditions was of interest to improve the precision and safety of chemotherapy [37–39]. Aiming at this challenge, the viability of FaDu cells was initially examined following 24 h of treatment with varying concentrations of PTX. Figure S16 showed that no obvious cell death was observed despite a slight decrease in cell viability with a gradual increase in PTX concentrations from 0 nM to 3.0 nM. A concentration of 3.0 nM PTX was chosen for the subsequent experiment. As observed in Fig. 5a, the fluorescence intensity of DCI-F-stained cells after pretreatment with low-dose PTX or L-RSL3 alone was marginally lower than that of the control group. Interestingly, the fluorescence intensity of cells pretreated with low-dose PTX in combination with L-RSL3 was dramatically lower than that of either the low-dose PTX or L-RSL3 group. Further, this fluorescence decrease was effectively suppressed upon the addition of Lip-1, demonstrating that this phenomenon was closely related to the ferroptosis process (Fig. 5a). The results revealed that there might be a potential synergistic antitumor effect between low-dose PTX and L-RSL3. Both of them enhanced the sensitivity of FaDu cells to chemotherapy by inducing ferroptosis and decreasing the intracellular GSH level. CCK-8 assays further verified this conclusion. Cell viability in the group co-treated with low-dose PTX and L-RSL3 was markedly lower than that of the group treated with either low-dose PTX or L-RSL3 alone, and the Lip-1 intervention partially recovered cell viability. Taken together, L-RSL3 could synergize with a non-cytotoxic dose of PTX to promote the death of FaDu cells and enhance the therapeutic effect through the ferroptosis mechanism.

3.6. Monitoring ferroptosis-enhanced chemotherapy in vivo and clinical specimens

Given that GSH levels in malignant tumor tissues were prominently higher than those in normal tissues, DCI-F could visualize tumor regions with the specific recognition of intracellular GSH. A FaDu tumor-bearing mouse model was established and divided into four experimental groups: control, PTX, RSL3, and a PTX+RSL3 combination group. As indicated in Fig. 6a, within 90 min post-intratumorally injection, the tumor area of control mice emitted intense fluorescence signals attributed to the high level of endogenous GSH within the tumor tissues. In comparison, the fluorescence intensity of the tumor area in the PTX group was weakened, and there was no statistical difference between

RSL3 and the control group. The fluorescence signals of the tumors in the PTX+RSL3 combination group were lower than those of the three groups mentioned above, suggesting that this combined treatment markedly reduced the GSH level in the tumor (Fig. 6b). The combination therapy group displayed better tumor suppression effects, and the variation of GSH levels in the tumor site could be dynamically imaged by DCI-F, thus realizing the visual tracing of the treatment process. Meanwhile, H&E staining results of the tumor tissues in each group further confirmed that the PTX+RSL3 group exhibited more pronounced structural disruption, verifying its enhanced anti-tumor effect (Fig. 6c). The above results indicated that DCI-F could be a powerful tool for HPC efficacy monitoring. To further validate the potential of DCI-F in clinical samples, fresh surgical specimens from HPC patients were collected and subjected to CLSM imaging (Fig. 6d). Tumor tissues were incubated with DCI-F for 30 min and then washed with PBS to remove non-specific binding. Clear fluorescence signals were detected up to a depth of 60 μm within the tumor tissues. The results demonstrated that DCI-F offered favorable imaging capabilities for intraoperative navigation and pathological evaluation in clinical HPC samples.

4. Conclusion

In summary, a NIRF probe DCI-F, was screened based on a substituent-regulation strategy to enable the visualization of intracellular GSH dynamics in the process of ferroptosis. DCI-F exhibited high sensitivity, fast response-ability, and excellent selectivity for GSH under physiological conditions. In particular, DCI-F could image GSH depletion in real-time during ferroptosis induced by the combination of low-dose PTX and RSL3. This combination strategy effectively overcame the potential toxicity problem associated with the use of PTX alone. DCI-F was also successfully applied to FaDu tumor-bearing mice model and HPC clinical specimens. Overall, DCI-F proved to be a promising tool for detecting GSH levels, with application in GSH-related disease diagnosis and therapeutic monitoring.

CRediT authorship contribution statement

Yongzhi Qi: Writing – original draft, Methodology, Data curation. Cuijuan Zhang: Writing – original draft, Methodology, Data curation. **Chenxiao Zhao**: Validation, Data curation. **Yuxia Zou**: Validation, Funding acquisition. **Ziyi Cheng**: Supervision, Funding acquisition. **Heng Liu**: Writing – review & editing, Supervision, Project administration, Funding acquisition, Conceptualization. **Xuejun Zhou**: Writing – review & editing, Supervision, Project administration, Funding acquisition, Conceptualization. **Fabiao Yu**: Writing – review & editing, Supervision, Project administration, Funding acquisition, Conceptualization.

Declaration of Competing Interest

The authors declare that they have no known competing financial interests or personal relationships that could have appeared to influence the work reported in this paper.

Acknowledgements

This work was supported by the National Natural Science Foundation of China (22461020, 82360504, 22264013, 82202647), Joint Program on Health Science & Technology Innovation of Hainan Province (WSJK2024MS240), Hainan Provincial Natural Science Foundation of China (822RC831, 825QN544), Scientific Research Project of Higher Education Institutions in Hainan Province (Hnky2024-38), Hainan Medical University Master Class A Project (HYYB2022A38), and Hainan Province Clinical Medical Center (2021). Thanks to the support and assistance in terms of instruments and facilities provided by Public Research Center of Hainan Medical University.

Appendix A. Supporting information

Supplementary data associated with this article can be found in the online version at doi:10.1016/j.snb.2025.138443.

Data availability

Data will be made available on request.

References

[1] F. Bray, M. Laversanne, H. Sung, J. Ferlay, R.L. Siegel, I. Soerjomataram, et al., Global cancer statistics 2022: globocan estimates of incidence and mortality worldwide for 36 cancers in 185 countries, CA Cancer J. Clin. 74 (2024) 229–263.
[2] N. Zidar, N. Gale, Update from the 5th edition of the world health organization classification of head and neck tumors: hypopharynx, larynx, trachea and parapharyngeal space, Head. Neck. Pathol. 16 (2022) 31–39.
[3] K.W. Lai, R. Lai, B.B. Lorincz, C.C. Wang, J.Y. Chan, D.C. Yeung, Oncological and functional outcomes of transoral robotic surgery and endoscopic laryngopharyngeal surgery for hypopharyngeal cancer: a systematic review, Front. Surg. 8 (2022) 810581.
[4] P.J. Bradley, Epidemiology of hypopharyngeal cancer, Adv. Otorhinolaryngol. 83 (2019) 1–14.
[5] J.D. Cramer, B. Burtness, Q.T. Le, R.L. Ferris, The changing therapeutic landscape of head and neck cancer, Nat. Rev. Clin. Oncol. 16 (2019) 669–683.
[6] S. Zhao, Y. Tang, R. Wang, M. Najafi, Mechanisms of cancer cell death induction by paclitaxel: an updated review, Apoptosis 27 (2022) 647–667.
[7] X. Jiang, The pharmacology of paclitaxel in cancer therapy, BIO Web Conf. EDP Sci. (2025) 02002.
[8] S. Rodrigues-Ferreira, H. Moindjie, M.M. Haykal, C. Nahmias, Predicting and overcoming taxane chemoresistance, Trends Mol. Med. 27 (2021) 138–151.
[9] E.V. Sazonova, G.S. Kopeina, E.N. Imyanitov, B. Zhivotovsky, Platinum drugs and taxanes: can we overcome resistance? Cell. Death. Discov. 7 (2021) 155.
[10] J. Li, F. Cao, H.-l Yin, Z.J. Huang, Z.T. Lin, N. Mao, et al., Ferroptosis: past, present and future, Cell. Death. Dis. 11 (2020) 88.
[11] X. Jiang, B.R. Stockwell, M. Conrad, Ferroptosis: mechanisms, biology and role in disease, Nat. Rev. Mol. Cell. Biol. 22 (2021) 266–282.
[12] D. Tang, X. Chen, R. Kang, G. Kroemer, Ferroptosis: molecular mechanisms and health implications, Cell. Res. 31 (2021) 107–125.
[13] W. Gao, X. Wang, Y. Zhou, X. Wang, Y. Yu, Autophagy, ferroptosis, pyroptosis, and necroptosis in tumor immunotherapy, Signal. Transduct. Tar. 7 (2022) 196.
[14] H. Xu, D. Ye, M. Ren, H. Zhang, F. Bi, Ferroptosis in the tumor microenvironment: perspectives for immunotherapy, Trends Mol. Med. 27 (2021) 856–867.
[15] J.A. Cook, D. Gius, D.A. Wink, M.C. Krishna, A. Russo, J.B. Mitchell, Oxidative stress, redox, and the tumor microenvironment. Semin. Radiat. Oncol, Elsevier, 2004, pp. 259–266.
[16] D. Gong, M. Chen, Y. Wang, J. Shi, Y. Hou, Role of ferroptosis on tumor progression and immunotherapy, Cell. Death. Discov. 8 (2022) 427.
[17] C. Zhang, X. Liu, S. Jin, Y. Chen, R. Guo, Ferroptosis in cancer therapy: a novel approach to reversing drug resistance, Mol. Cancer 21 (2022) 47.
[18] C. Ding, T. Ren, Near infrared fluorescent probes for detecting and imaging active small molecules, Coord. Chem. Rev. 482 (2023) 215080.
[19] Y.L. Qi, Y.Z. Li, M.J. Tan, F.F. Yuan, N. Murthy, Y.T. Duan, et al., Recent advances in organic near-infrared ratiometric small-molecule fluorescent probes, Coord. Chem. Rev. 486 (2023) 215130.
[20] Z. Zeng, S.S. Liew, X. Wei, K. Pu, Hemicyanine-based near-infrared activatable probes for imaging and diagnosis of diseases, Angew. Chem. Int. Ed. 60 (2021) 26454–26475.
[21] S. He, P. Cheng, K. Pu, Activatable near-infrared probes for the detection of specific populations of tumour-infiltrating leukocytes in vivo and in urine, Nat. Biomed. Eng. 7 (2023) 281–297.
[22] Q. Zeng, Z. Yuwen, L. Zhang, Y. Li, H. Liu, K. Zhang, Molecular engineering of a doubly quenched fluorescent probe enables ultrasensitive detection of biothiols in highly diluted plasma and high-fidelity imaging of dihydroartemisinin-induced ferroptosis, Anal. Chem. 96 (2024) 13260–13269.
[23] L.L. Wang, Q. Xu, Y.Z. Xie, Y.R. Zhang, M.H. Zheng, X.F. Li, et al., A triple-targeting fluorescent probe reveals the glutathione and viscosity crosstalk in mitochondria, endoplasmic reticulum, and nucleoli in cells during ferroptosis, Sens. Actuat. B Chem. 399 (2024) 134872.
[24] Z.C. Yang, Q.S. Gu, J.J. Chao, F.Y. Tan, G.J. Mao, L. Hu, et al., Glutathione-activated biotin-targeted dual-modal imaging probe with improved pdt/ptt synergistic therapy, Anal. Chim. Acta 1316 (2024) 342860.
[25] Y. Wang, G. Zhao, Y. Liu, R. Wang, Y. Xing, K. Dou, et al., Glutathione-activated near-infrared ii fluorescent probe for lung metastatic diagnosis and intraoperative imaging of tumor, Sens. Actuat. B Chem. 426 (2025) 137005.
[26] G. Suna, S. Topal, E. Karakuş, Selective and sensitive detection of glutathione with a novel fluorescein-based probe in fully aqueous media and its application in food samples, Dyes Pigments 234 (2025) 112551.
[27] H. Tan, M. Zeng, C. Fang, X. Zhu, M. Liu, Y. Long, et al., A glutathione-sensitive small molecule fluorescent probe for rapid and facile gut microbiota sensing, Spectrochim. Acta A. 327 (2025) 125408.

[28] W. Zhang, M. Zhang, M. Li, X. Wang, P. Li, B. Tang, Glutathione and viscosity double-locked response fluorescent probe for imaging and surgical navigation of hepatocellular carcinoma, Chem. Commun. 60 (2024) 10021–10024.
[29] X. Song, X. Wang, Y. Wang, Y. Hao, C. Li, L. Chai, et al., Monitoring glutathione content of the endoplasmic reticulum under scrap leather-induced endoplasmic reticulum stress via an endoplasmic reticulum-targeted two-photon fluorescent probe, Anal. Chem. 96 (2024) 18132–18140.
[30] T. Liu, Y. Li, L. Mi, Y. Wei, Y. Zhang, W. Mao, Sequential activation strategy of triazinyl resorufin for high selectivity fluorescence GSH detection, Talanta 269 (2024) 125477.
[31] R. He, D. Tang, N. Xu, H. Liu, K. Dou, X. Zhou, et al., Evaluation of erastin synergized cisplatin anti-nasopharyngeal carcinoma effect with a glutathione-activated near-infrared fluorescent probe, Chin. Chem. Lett. 35 (2024) 108658.
[32] Y. Wang, Y. Li, J. Cao, X. Yang, J. Huang, M. Huang, et al., Research progress of fluorescent probes for detection of glutathione (gsh): fluorophore, photophysical properties, biological applications, Molecules 29 (2024) 4333.
[33] S. Li, Y. Liu, J. Li, X. Zhao, D. Yu, Mechanisms of ferroptosis and application to head and neck squamous cell carcinoma treatments, DNA. Cell. Biol. 40 (2021) 720–732.
[34] W. Zhang, Y. Liu, Y. Liao, C. Zhu, Z. Zou, Gpx4, ferroptosis, and diseases, Biomed. Pharm. 174 (2024) 116512.
[35] Q. Zhou, Y. Meng, D. Li, L. Yao, J. Le, Y. Liu, et al., Ferroptosis in cancer: from molecular mechanisms to therapeutic strategies, Signal. Transduct. Tar. 9 (2024) 55.
[36] A. Birnbaum, T. Dipetrillo, R. Rathore, E. Anderson, H. Wanebo, Y. Puthwala, et al., Cetuximab, paclitaxel, carboplatin, and radiation for head and neck cancer: a toxicity analysis, Am. J. Clin. Oncol. 33 (2010) 144–147.
[37] G. Yang, W. Li, H. Jiang, X. Liang, Y. Zhao, D. Yu, et al., Low-dose radiation May be a novel approach to enhance the effectiveness of cancer therapeutics, Int. J. Cancer. 139 (2016) 2157–2168.
[38] J. Lötsch, G. Geisslinger, Low-dose drug combinations along molecular pathways could maximize therapeutic effectiveness while minimizing collateral adverse effects, Drug. Discov. Today 16 (2011) 1001–1006.
[39] J. Ye, X. Jiang, Z. Dong, S. Hu, M. Xiao, Low-concentration ptx and rsl3 inhibits tumor cell growth synergistically by inducing ferroptosis in mutant p53 hypopharyngeal squamous carcinoma, Cancer. Manag. Res. 11 (2019) 9783–9792.

Yongzhi Qi is a master's degree student at Hainan Medical University.

Cuijuan Zhang is a supervisor nurse at the First Medical Center of the General Hospital of the People's Liberation Army.

Chenxiao Zhao is a master's degree student at Hainan Medical University.

Yuxia Zou is an attending doctor at the Department of Otolaryngology, Head and Neck Surgery, the First Affiliated Hospital of Hainan Medical University. His research interests focus on optical diagnosis.

Ziyi Cheng is an associate professor at Hainan Medical University. His research interests focus on optical diagnosis.

Heng Liu is a professor at Hainan Medical University. He received his Ph.D. degree from the University of Chinese Academy of Sciences in 2014. His research interests included the development of fluorescent probes and advanced molecular imaging agents.

Xuejun Zhou is a senior doctor at the First Affiliated Hospital of Hainan Medical University. He received his Ph.D. degree from Xinjiang Medical University in 2006. His research interests focus on the diagnosis and treatment of otolaryngology-related diseases.

Fabiao Yu is a professor at Hainan Medical University. Her research interests included the development of fluorescent probes and advanced molecular imaging agents.